The Impact of Motion Artifacts on Transcutaneous Oxygen Measurements

Vladimir Vakhter*‡, Burak Kahraman*‡, Guixue Bu†, Foroohar Foroozan†, Beth A. Beidleman§, and Ulkuhan Guler*
*Department of Electrical and Computer Engineering, Worcester Polytechnic Institute, Worcester, MA 01609 USA
†Analog Devices Inc., Wilmington, MA 01887 USA
§ United States Army Research Institute of Environmental Medicine, Natick, MA 01887 USA

2023 IEEE Biomedical Circuits and Systems Conference (BioCAS) | 979-8-3503-0026-0/23/$31.00 ©2023 IEEE | DOI: 10.1109/BioCAS58349.2023.10388659

***Abstract*—Transcutaneous oxygen monitoring is a noninvasive method of measuring the partial pressure of oxygen permeating through the skin ($PtcO_2$). Its medical significance lies in correlating changes in $PtcO_2$ with alterations in arterial oxygen levels. Luminescent lifetime-based oxygen sensing is suitable for measuring $PtcO_2$ with miniaturized systems like wearables, where a consistent and reliable signal is crucial for accurate measurements. This study presents the preliminary results of examining the impact of motion artifacts on $PtcO_2$ measurements based on the luminescent lifetime-based technique. To conduct these tests, a custom wearable $PtcO_2$ monitor was used, and its onboard accelerometer was calibrated. The study included two human subjects who executed basic forearm movements (lateral and medial rotations and flexion). The pilot tests showed that the luminescent lifetime-based technique is notably resilient against motion artifacts, as the change in lifetime values during motions did not exceed 4%. Importantly, we believe this study is the first in the literature to specifically investigate the impact of motion artifacts on the lifetime-based $PtcO_2$ measurements through human tests.**

I. Introduction

The transcutaneous partial pressure of oxygen ($PtcO_2$) is a noninvasive measure that assesses the amount of oxygen diffusing from the capillaries through the skin surface [1], [2]. $PtcO_2$ serves as an indicator of the skin's metabolic state, reflecting the balance between oxygen delivery and local tissue demands. Additionally, it provides valuable insights into the microcirculatory condition beneath the skin [3], [4]. Furthermore, it is considered a reliable indicator of changes in the arterial partial pressure of oxygen (PaO_2) in patients with normal cardiovascular function [5]–[7].

Monitoring $PtcO_2$ is vital across a wide range of medical scenarios [8], [9]. One significant use case is the early detection of pulmonary diseases [10], [11] — such as chronic obstructive pulmonary disease (COPD), the coronavirus disease of 2019 (COVID-19), and lower respiratory disease — which are among the top leading causes of death worldwide [12], [13]. Additionally, $PtcO_2$ monitoring is valuable for assessing respiratory distress, a common reason for infant admission to neonatal intensive care units (NICU) [14]. It also aids in diagnosing peripheral arterial insufficiency (restricted blood flow to the limbs) [15], [16]. Moreover, $PtcO_2$ monitoring is used in assessing the severity of ischemia [17], evaluating the wound healing potential [18]–[21], or determining the optimal amputation level [22].

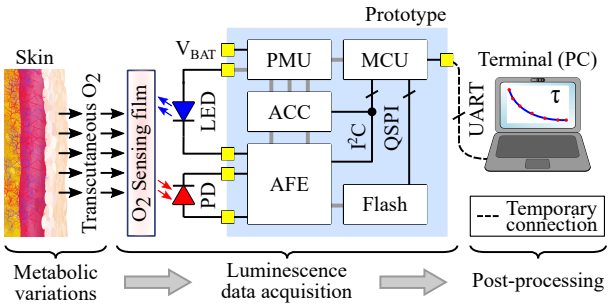

Fig. 1: Functional block diagram of the $PtcO_2$ monitoring system (I^2C - Inter-Integrated Circuit, QSPI - Quad Serial Peripheral Interface, and UART - Universal Asynchronous Receiver-Transmitter).

Researchers have been investigating the luminescence-based oxygen-sensing method to create compact wearables for continuous monitoring of $PtcO_2$ [23]–[28]. In this technique, a light-emitting diode (LED) excites a luminescent sensing film. The optical response of the film, including intensity and lifetime (τ), is captured by a photodiode (PD), processed with a specialized analog front end (AFE), and digitized by an analog-to-digital converter (ADC) (as shown in Fig. 1). The film is designed with the use of a special luminophore — such as platinum porphyrin (Pt-porphyrin) [29] — which exhibits luminescence quenching when oxygen is present. The luminescence intensity and lifetime are inversely proportional to the partial pressure of oxygen (PO_2) [30]. Compared to the intensity-based method, the lifetime-based method is more reliable being less affected by changes in the optical path and excitation strength [27]. More information about the operation principle of the luminescence-based oxygen-sensing method can be found in [31].

From a health care provider perspective, the signal quality of wearable $PtcO_2$ monitors is crucial [32], [33] since inaccurate measurements can lead to incorrect diagnoses and treatments [34], [35]. A practical wearable $PtcO_2$ monitor should demonstrate resilience against motion artifacts to ensure accurate measurements, even when capturing subtle variations (on the order of nanoseconds) in lifetime values outside of

Vladimir Vakhter‡ and Burak Kahraman‡ contributed equally to this work. This material is based upon work supported in part by the National Science Foundation (NSF) under Grant OAC-2203827, the United States Army Research Institute of Environmental Medicine (USARIEM) under Grant HT942523P0008 and Analog Devices Inc. (ADI) through a research gift. Corresponding author: Ulkuhan Guler: uguler@wpi.edu.

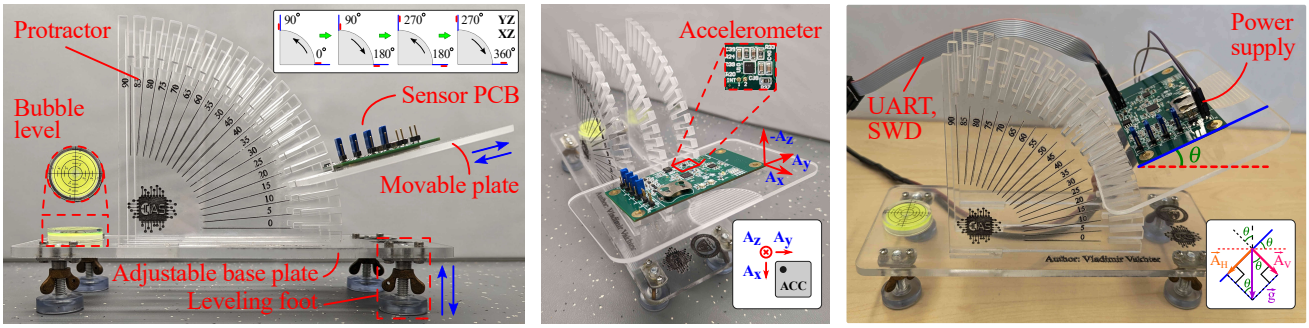

(a) (b) (c)

Fig. 2: Accelerometer calibration setup: (a) front view (the inset graph exemplifies calibration for both the YZ and XZ planes, where the PCB is shown in blue and the accelerometer is shown in red), (b) isometric view (the inset graph shows axes of acceleration sensitivity A_x, A_y, and A_z relative to the first pin of the accelerometer (ACC)), and (c) the sensor under test (the inset graph illustrates how the reference acceleration data was calculated).

laboratory settings [36], [37]. In such cases, motion artifacts become the primary source of noise and can significantly degrade the signal quality, rendering $PtcO_2$ measurements clinically unreliable [34], [38], [39].

In this study, we conducted preliminary tests on human subjects to examine the impact of motion artifacts on $PtcO_2$ measurements. We utilized a prototype of the wearable monitor, described in [28], which incorporates an onboard accelerometer to detect body movements during data acquisition. The remainder of this paper is organized as follows. Section II introduces the prototype utilized in the experiments. Section III elaborates on the procedure and results of the accelerometer calibration. Section IV provides the details and results of the human subject tests. Finally, Section V concludes the paper.

II. System Architecture

Our custom wearable $PtcO_2$ monitor, implemented on a rigid printed circuit board (PCB) and shown in Fig. 1, comprises six primary hardware blocks: (1) a power management unit (PMU) — including two switching regulators [40], [41] — supplying other blocks in the system from an external power source (such as a lithium coin cell battery [42]); (2) a sensor head optically exciting the O_2-sensing film [29] with a blue LED (with a peak wavelength λ of 450 nm) [43] and capturing its luminescent response using a red PD (with an integrated bandpass filter with the peak sensitivity at λ of 600 nm) [44]; (3) an AFE [45] — working in the impulse response mode [32] — driving the LED and capturing and digitizing the photocurrent of PD; (4) an accelerometer (ACC) [46] detecting body movements; (5) a 4 MB Flash memory [47] retaining measurement results; and (6) a microcontroller unit (MCU) [48] controlling the PMU, retrieving data from the accelerometer, processing the data from AFE, storing this data to the external Flash, and sending it to a terminal — a personal computer (PC) — at the end of a measurement.

The primary firmware logic remains unchanged from our previous work [28]. However, for each decay curve, we also record acceleration data. Instead of being transmitted to the terminal, the data is stored in the onboard Flash memory. In addition, no averaging of decay curves is performed to address the sensitivity of the accelerometer and the potential for significant changes in the human subject's position between subsequent AFE measurements. The τ values are extracted from the collected decay curves in MATLAB as described in [28]. Additional information on the system architecture can be found in [27], [28].

III. Calibration of Accelerometer

This section presents the technique and the setup utilized to calibrate the accelerometer, as well as the calibration results.

A. Setup

The calibration setup for the accelerometer is depicted in Fig. 2. To ensure that the base plate is aligned perpendicular to the vector of gravitational acceleration, the leveling feet and bubble level are utilized. The alignment is considered achieved when the bubble and the circle on the level become concentric. The protractor features a set of slots positioned at 5° intervals, spanning from 0° to 90°. The PCB is affixed to a movable plate that can be inserted into the protractor's slots.

B. Procedure

To establish a calibration profile encompassing the complete range of motions from 0° to 360°, we used a quarter circle (90°) and rotated/flipped the PCB relative to the protractor's slots. As we adjusted the position of the PCB, we collected the data obtained from the accelerometer's output at various angles for each axis of acceleration sensitivity, as exemplified in the inset graph in Fig. 2a. To calibrate all three axes of acceleration sensitivity (as depicted in the inset graph in Fig. 2b), we first used the Y-axis as the rotation axis to obtain the data for the XZ plane. Subsequently, we utilized the X-axis as the rotation axis to collect the data for the YZ plane.

For each plane, we calculated the reference data using the following equation:

$$\begin{bmatrix} A_{H,\mathrm{REF}} \\ A_{V,\mathrm{REF}} \end{bmatrix} = \begin{bmatrix} |\vec{g}| \cdot \sin\theta \\ |\vec{g}| \cdot \cos\theta \end{bmatrix}, \tag{1}$$

where $|\vec{g}|$ is the absolute value of the vector of gravitational acceleration, $A_{H,\mathrm{REF}}$ is the horizontal component of acceleration (parallel to the surface of the accelerometer), $A_{V,\mathrm{REF}}$ is the vertical component of acceleration (perpendicular to the surface of the accelerometer), and θ is the rotation angle, as illustrated in the inset graph in Fig 2c.

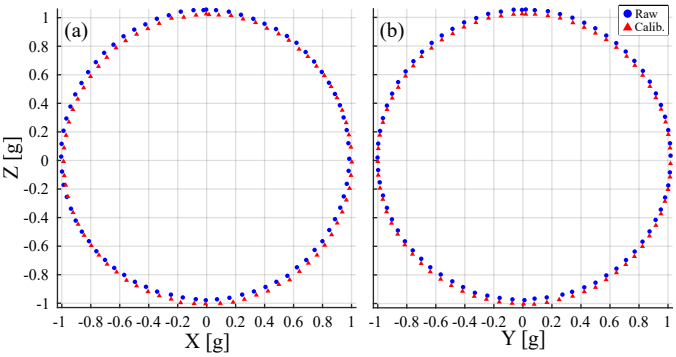

Fig. 3: Measurement results for the accelerometer before (blue) and after (red) calibration: (a) in the XZ plane and (b) in the YZ plane.

Equation (1) represents an ideal circle with a radius of $|\vec{g}|$. For each angle step (5°), we computed the average of ten measurements and determined the difference between the obtained value and the reference value. After covering the entire range from 0° to 360°, we calculated the average of all the individual differences. This way, we derived the calibration coefficients for all three axes of acceleration sensitivity, which were stored in the accelerometer to enable data correction.

C. Results

After calibrating the accelerometer, we repeated the measurements spanning the entire range from 0° to 360°, with a 5° increment. The results obtained before and after calibration are shown in Fig. 3. We calculated the root mean square errors (RMSE) of the pairwise differences between the reference dataset and each of the raw and calibrated datasets using the following equation:

$$\text{RMSE} = \sqrt{\sum_{i=1}^{n} \frac{(g_{\text{meas},i} - g_{\text{ref},i})^2}{n}}, \tag{2}$$

where n is the dataset size, $g_{\text{meas},i}$ is the i-th measured acceleration value for a particular axis (X, Y, or Z), and $g_{\text{ref},i}$ is the corresponding i-th reference acceleration value. As seen in Table I, the calibration improved the measurement precision.

TABLE I
RMSE Values of the Raw and Calibrated Acceleration Data

Axis	Raw	Calibrated	% Improvement
X	0.0143	0.0119	16.8
Y	0.0105	0.0100	4.8
Z	0.0369	0.0179	51.5

IV. Human Subject Tests

This section outlines the procedures implemented for conducting human subject tests along with the corresponding results. The Institutional Review Board of Worcester Polytechnic Institute approved the study protocol (IRB-22-0682). Verbal consent was obtained from all human research participants (one male and one female). The research was performed in accordance with the Declaration of Helsinki [49].

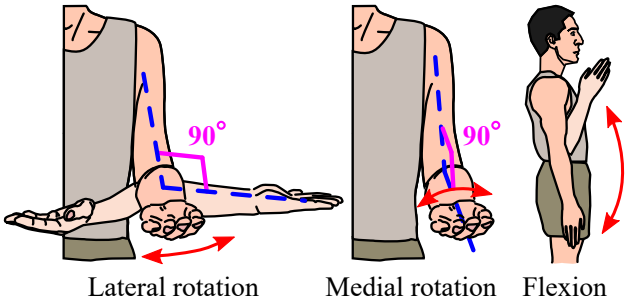

Fig. 4: Motion types.

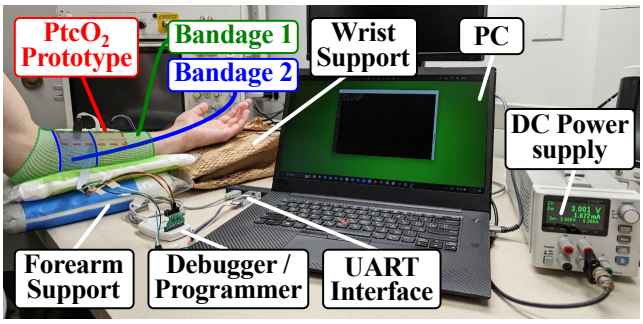

Fig. 5: The materials and equipment used for human subject tests.

A. Motion Artifact Experiments

These experiments involved three distinct types of motion: lateral rotation of the forearm, flexion of the elbow joint, and medial rotation of the forearm (with the palm facing upwards-downwards), as illustrated in Fig. 4. We recorded decay curves every 463 ms. The total duration of the experiment for each human subject was 76 minutes. In each experiment, there was a stabilization phase lasting $\sim$ 40 minutes, where the oxygen in the sensing film stabilized with the oxygen diffusing through the skin [50]. In this phase, decay curves were collected only within the last 20 minutes. The stabilization phase was followed by the motion phase lasting 36 minutes. During this phase, participants performed each of the mentioned motion types for 2 minutes, followed by a 10-minute rest period.

For these experiments, we utilized the components shown in Fig. 5. We securely affixed the prototype on the subject's forearm using elastic net tubular bandages. We selected the bandages with appropriate elastic properties to ensure that they did not cause occlusion to the subject's arm. During the stabilization phase and the rest periods within the motion phase, the human subject sat in a chair and kept their forearm in a fixed position, attempting to maintain the acceleration in the Z-axis equal to 1 $\vec{g}$ while accelerations in both the X and Y directions were equal to zero. This was achieved using forearm support and wrist support, as illustrated in Fig. 5. During the motion phase, the human subject stood while holding and moving their hand, as shown in Fig. 4. The measurement setup comprised several additional components, including a debugger/programmer utilized for programming the MCU and a UART interface connected to the terminal (PC) for retrieving the data stored in the Flash at the end of measurements, enabling post-processing in MATLAB. Additionally, a DC

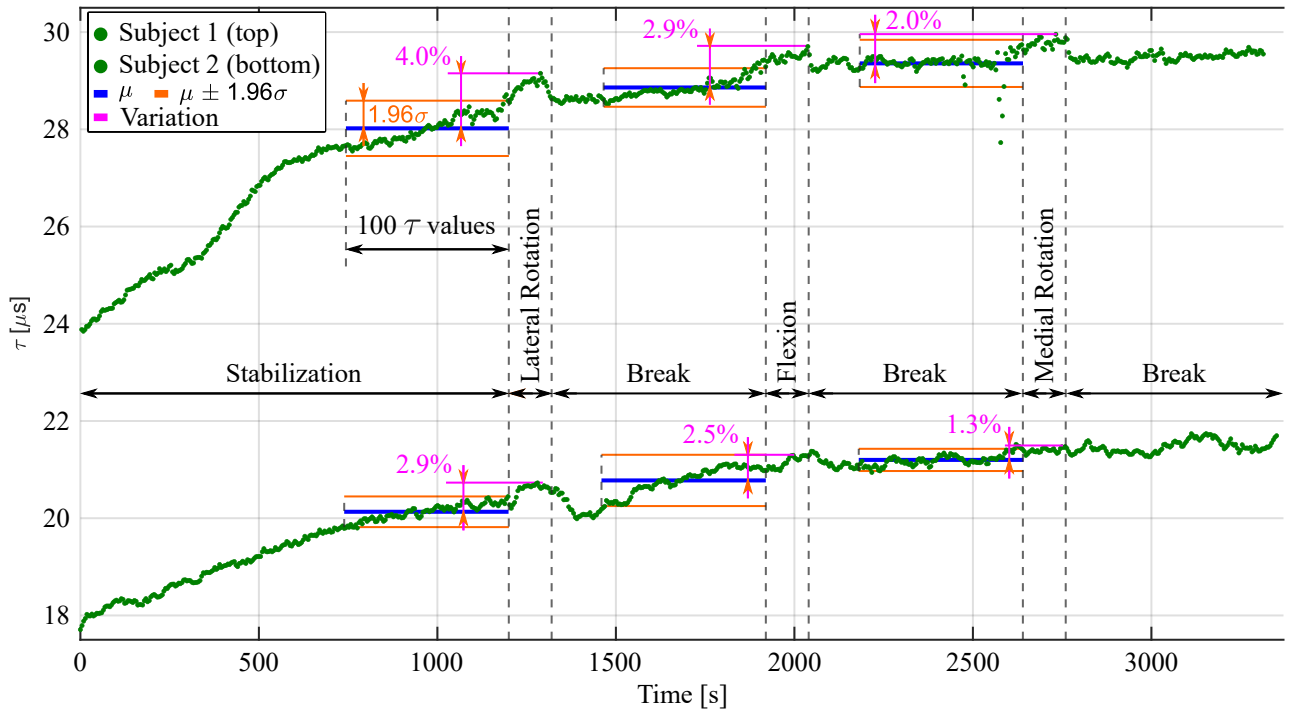

Fig. 6: Measurement results of the human subject tests (where μ and σ denote the mean and the standard deviation of the 100 τ values before the start of motion, respectively).

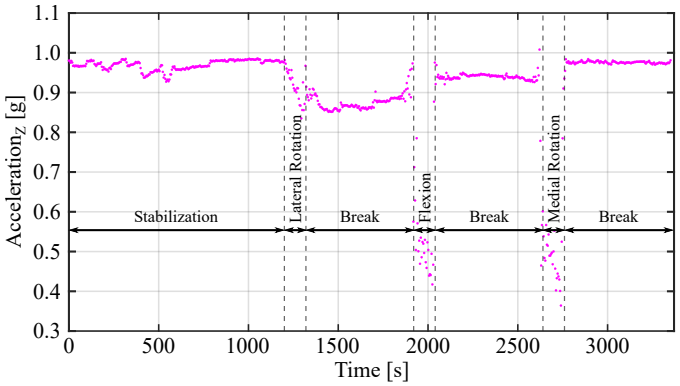

Fig. 7: An example graph depicting the Z-axis acceleration for subject 2.

power supply remained connected to the sensing prototype throughout the experiment.

B. Results and Discussion

The results of the motion artifact experiments are demonstrated in Fig. 6 while an example acceleration data is displayed in Fig. 7 to show that the motion artifacts are present during the indicated intervals. We observed a similar trend in τ for both subjects. The variations of τ are shown in Table II.

We calculated the mean (μ) and standard deviation (σ) of the 100 τ values prior to motions, as well as the deviation of the maximum τ value during motion from μ. The lateral rotation of the forearm was found to result in the largest variation of τ, while the medial rotation resulted in the smallest variation. However, the fluctuations in τ values are not solely attributable to motion artifacts. They also signify the ongoing process of settling τ values in both subjects. From our previous study [50], the settlement time of τ values varied from 1251 s

TABLE II
Variation of τ in motion artifact experiments for human subjects 1 and 2

Subject	μ^*	**Variation†**	μ^*	**Variation†**	μ^*	**Variation†**
1	28	4	28.9	2.9	29.4	2
2	20.1	2.9	20.8	2.5	21.2	1.3
Phase	Lateral rotation		Flexion		Medial rotation	

Note(s): * - mean value in μs. † - % variation.

to 5133 s without heating. Additionally, these variations can be influenced by the limitations of the rigid prototype. To improve measurements, the wearable prototype should be miniaturized and encapsulated in a medical-grade quality package.

V. Conclusion

In this study, we present the results of the preliminary tests investigating the impact of motion artifacts on transcutaneous oxygen measurements. To achieve this, we employed a custom transcutaneous oxygen monitor equipped with an accurately calibrated onboard accelerometer for motion tracking. Our study involved a small human cohort, wherein basic forearm movements were performed. The results indicated that the variation in lifetime values during motions remained within a 4% range, demonstrating the robustness of the luminescent lifetime-based technique against motion artifacts. Additional studies should determine the impact of motion artifacts on transcutaneous oxygen measurements and the optimal signal quality index (SQI) for assessing $\mathrm{PtcO_2}$ signals [51]. Based on this SQI, an adaptive algorithm to remove motion artifacts from the $\mathrm{PtcO_2}$ signals should be developed [34]. To the best of our knowledge, this work represents the first coverage of this topic in the literature for luminescent lifetime-based oxygen sensing.

REFERENCES

[1] Y. Mendelson and R. A. Peura, "Noninvasive transcutaneous monitoring of arterial blood gases," *IEEE Transactions on Biomedical Engineering*, no. 12, pp. 792–800, 1984.

[2] U. Franzeck *et al.*, "Microangiopathy of cutaneous blood and lymphatic capillaries in chronic venous insufficiency (CVI)." *The Yale Journal of Biology and Medicine*, vol. 66, no. 1, p. 37, 1993.

[3] L. John *et al.*, "Transcutaneous partial pressure of oxygen measurement in advanced chronic venous insufficiency as a marker of tissue oxygenation," *Vascular Specialist International*, vol. 37, 2021.

[4] R. A. Mohd Rashid *et al.*, "Transcutaneous oxygen pressure monitoring ($TcPO_2$). Technology Review." *Ministry of Health Malaysia: Malaysian Health Technology Assessment Section (MaHTAS)*, pp. 1–47, 2022.

[5] R. A. White *et al.*, "Noninvasive evaluation of peripheral vascular disease using transcutaneous oxygen tension," *The American Journal of Surgery*, vol. 144, no. 1, pp. 68–75, 1982.

[6] H. P. Wiedemann *et al.*, "Transcutaneous oxygen monitoring," *Cleveland Clinic Quarterly*, vol. 52, no. 4, pp. 483–488, 1985.

[7] M. Franklin, "Transcutaneous measurement of partial pressure of oxygen and carbon dioxide." *Respiratory Care Clinics of North America*, vol. 1, no. 1, pp. 119–131, 1995.

[8] Perimed, "Transcutaneous oximetry ($tcPO_2$)," [Online]. Available: https://www.perimed-instruments.com/content/transcutaneous-oximetry-tcpo2/, Aug 2022.

[9] A. Y. Mousa and J. L. Ballard, "Transcutaneous oxygen tension: Principles and applications," in *Noninvasive Vascular Diagnosis: A Practical Textbook for Clinicians*. Springer, 2021, pp. 1–16.

[10] U. Guler *et al.*, "Emerging blood gas monitors, how they can help with COVID-19," *IEEE Solid-State Circuits Magazine*, vol. 12, no. 4, pp. 33–47, 2020.

[11] I. Costanzo *et al.*, "Respiratory monitoring: Current state of the art and future roads," *IEEE Reviews in Biomedical Engineering*, vol. 15, pp. 103–121, 2022.

[12] *World Health Organization*: The top 10 causes of death, [Online]. Available: https://www.who.int/news-room/fact-sheets/detail/the-top-10-causes-of-death. [Accessed Jan.26, 2023].

[13] *World Health Organization*: Coronavirus (COVID-19) Dashboard, [Online]. Available: https://covid19.who.int. [Accessed Jan.26, 2023].

[14] U. Guler *et al.*, "Sensors for Neonatal Monitoring," in *Reference Module in Biomedical Sciences*. Elsevier, Jan. 2022.

[15] P. Byrne *et al.*, "The use of transcutaneous oxygen tension measurements in the diagnosis of peripheral vascular insufficiency." *Annals of surgery*, vol. 200, no. 2, p. 159, 1984.

[16] L. Lusiani *et al.*, "Transcutaneous oxygen tension (tcpo2) measurement as a diagnostic tool in patients with peripheral vascular disease," *Angiology*, vol. 39, no. 10, pp. 873–880, 1988.

[17] H. H. Moosa *et al.*, "Transcutaneous oxygen measurements in lower extremity ischemia: effects of position, oxygen inhalation, and arterial reconstruction," *Surgery*, vol. 103, no. 2, pp. 193–198, 1988.

[18] K. A. Arsenault *et al.*, "The use of transcutaneous oximetry to predict complications of chronic wound healing: A systematic review and meta-analysis," *Wound Repair Regen*, vol. 19, no. 6, pp. 657–663, 2011.

[19] K. L. Andrews *et al.*, "Noninvasive arterial studies including transcutaneous oxygen pressure measurements with the limbs elevated or dependent to predict healing after partial foot amputation," *Am J Phys Med & Rehabi*, vol. 92, no. 5, pp. 385–392, 2013.

[20] J. H. Niinikoski, "Clinical hyperbaric oxygen therapy, wound perfusion, and transcutaneous oximetry," *World journal of surgery*, vol. 28, pp. 307–311, 2004.

[21] D. Mathieu *et al.*, "Post-traumatic limb ischemia: prediction of final outcome by transcutaneous oxygen measurements in hyperbaric oxygen." *The Journal of trauma*, vol. 30, no. 3, pp. 307–314, 1990.

[22] C. Wyss *et al.*, "Transcutaneous oxygen tension as a predictor of success after an amputation." *JBJS*, vol. 70, no. 2, pp. 203–207, 1988.

[23] C.-J. Lim *et al.*, "Wearable, luminescent oxygen sensor for transcutaneous oxygen monitoring," *ACS Applied Materials & Interfaces*, vol. 10, no. 48, pp. 41 026–41 034, Jul. 2018.

[24] I. Costanzo *et al.*, "A prototype towards a transcutaneous oxygen sensing wearable," in *IEEE Biomedical Circuits and Systems Conference (BioCAS)*, Oct. 2019, pp. 1–4.

[25] I. Costanzo *et al.*, "Fluorescent intensity and lifetime measurement of platinum-porphyrin film for determining the sensitivity of transcutaneous oxygen sensor," in *IEEE International Symposium on Circuits and Systems (ISCAS)*, Oct. 2020, pp. 1–5.

[26] I. Costanzo *et al.*, "An integrated readout circuit for a transcutaneous oxygen sensing wearable device," in *2020 IEEE Custom Integrated Circuits Conference (CICC)*, Mar. 2020, pp. 1–4.

[27] B. Kahraman et al., "A miniaturized prototype for continuous noninvasive transcutaneous oxygen monitoring," *2022 IEEE Biomedical Circuits and Systems Conference (BioCAS)*, pp. 486–490, 2022.

[28] V. Vakhter *et al.*, "A prototype wearable device for noninvasive monitoring of transcutaneous oxygen," *IEEE Transactions on Biomedical Circuits and Systems*, 2023.

[29] *Ocean Optics Inc. RedEye Oxygen Sensor Patches*, 2019. [Online]. Available: https://oceanoptics.com/product/redeye-oxygen-sensing-patches/. [Accessed Sep.29, 2019].

[30] M. Quaranta *et al.*, "Indicators for optical oxygen sensors," *Bioanalytical Reviews*, vol. 4, no. 2-4, p. 115, Dec 2012.

[31] I. Costanzo *et al.*, "A noninvasive miniaturized transcutaneous oxygen monitor," *IEEE Transactions on Biomedical Circuits and Systems*, vol. 15, no. 3, pp. 474–485, Jun. 2021.

[32] B.Kahraman *et al.*, "Power and accuracy optimization for luminescent transcutaneous oxygen measurements," *IEEE International Symposium on Circuits and Systems (ISCAS)*, pp. 1–4, 2022.

[33] I. Costanzo *et al.*, "A nonuniform sampling lifetime estimation technique for luminescent oxygen measurements," *European Solid State Circuits Conference (ESSCIRC)*, 2022.

[34] R. Yousefi *et al.*, "A motion-tolerant adaptive algorithm for wearable photoplethysmographic biosensors," *IEEE journal of biomedical and health informatics*, vol. 18, no. 2, pp. 670–681, 2013.

[35] X. Ding *et al.*, "Wearable sensing and telehealth technology with potential applications in the coronavirus pandemic," *IEEE reviews in biomedical engineering*, vol. 14, pp. 48–70, 2020.

[36] P. Bonato, "Wearable sensors and systems," *IEEE Engineering in Medicine and Biology Magazine*, vol. 29, no. 3, pp. 25–36, 2010.

[37] E. Jovanov and A. Milenkovic, "Body area networks for ubiquitous healthcare applications: opportunities and challenges," *Journal of medical systems*, vol. 35, pp. 1245–1254, 2011.

[38] H. Banaee *et al.*, "Data mining for wearable sensors in health monitoring systems: a review of recent trends and challenges," *Sensors*, vol. 13, no. 12, pp. 17 472–17 500, 2013.

[39] M. M. Baig *et al.*, "A systematic review of wearable patient monitoring systems–current challenges and opportunities for clinical adoption," *Journal of medical systems*, vol. 41, pp. 1–9, 2017.

[40] "MAX17225 datasheet and product info," [Online]. Available: https://www.analog.com/en/products/max17225.html.

[41] "ADM7160 datasheet and product info," [Online]. Available: https://www.analog.com/en/products/adm7160.html.

[42] *Energizer* CR2032: product datasheet, [Online]. Available: https://data.energizer.com/pdfs/cr2032.pdf. [Accessed Dec.5, 2022].

[43] "LXZ1-PR01 datasheet and product info," [Online]. Available: https://lumileds.com/products/color-leds/luxeon-z-colors/.

[44] "SD019-141-411-R datasheet and product info," [Online]. Available: https://www.advancedphotonix.com/product/detectors/photodiodes/.

[45] "ADPD4101 datasheet and product info," [Online]. Available: https://www.analog.com/en/products/adpd4101.html.

[46] "ADXL367 datasheet and product info," [Online]. Available: https://www.analog.com/en/products/adxl367.html.

[47] "W25Q32JVSSIQ datasheet and product info," [Online]. Available: https://www.winbond.com/hq/support/documentation/levelOne.jsp?__locale=en&DocNo=DA00-W25Q32JV.1.

[48] "STM32WB35CC datasheet and product info," [Online]. Available: https://www.st.com/en/microcontrollers-microprocessors/stm32wb35cc.html.

[49] *World Medical Association* Declaration of Helsinki: Ethical principles for medical research involving human subjects, [Online]. Available: https://www.wma.net/policies-post/wma-declaration-of-helsinki-ethical-principles-for-medical-research-involving-human-subjects/. [Accessed Dec.6, 2022].

[50] A. Leonardi *et al.*, "Optimizing transcutaneous oxygen measurement sites on humans," *2023 45th Annual International Conference of the IEEE Engineering in Medicine Biology Society (EMBC)*, pp. 1–4, 2023.

[51] M. Elgendi, "Optimal signal quality index for photoplethysmogram signals," *Bioengineering*, vol. 3, no. 4, p. 21, 2016.